How superhydrophobicity breaks down

Periklis Papadopoulos, Lena Mammen, Xu Deng, Doris Vollmer[1], and Hans-Jürgen Butt

Physics at Interfaces, Max Planck Institute for Polymer Research, D-55128 Mainz, Germany

Edited by Pablo Gaston Debenedetti, Princeton University, Princeton, NJ, and approved January 4, 2013 (received for review October 25, 2012)

A droplet deposited or impacting on a superhydrophobic surface rolls off easily, leaving the surface dry and clean. This remarkable property is due to a surface structure that favors the entrainment of air cushions beneath the drop, leading to the so-called Cassie state. The Cassie state competes with the Wenzel (impaled) state, in which the liquid fully wets the substrate. To use superhydrophobicity, impalement of the drop into the surface structure needs to be prevented. To understand the underlying processes, we image the impalement dynamics in three dimensions by confocal microscopy. While the drop evaporates from a pillar array, its rim recedes via stepwise depinning from the edge of the pillars. Before depinning, finger-like necks form due to adhesion of the drop at the pillar's circumference. Once the pressure becomes too high, or the drop too small, the drop slowly impales the texture. The thickness of the air cushion decreases gradually. As soon as the water–air interface touches the substrate, complete wetting proceeds within milliseconds. This visualization of the impalement dynamics will facilitate the development and characterization of superhydrophobic surfaces.

micropillars | pinning | wetting transition | contact angle | lithography | self-cleaning | hysteresis

Many surfaces in nature, including several plant leaves (1), legs of the water striders (2), and the wings of some insects (3, 4) are superhydrophobic. They display apparent contact angles with water greater than 150° and low contact angle hysteresis (1–4). Tilting a superhydrophobic surface by a few degrees is already sufficient for a drop to overcome adhesion, roll off, and remove dirt (1–4). This has stimulated extensive research to design artificial superhydrophobic surfaces. A variety of techniques are developed, often stimulated by mimicking natural surfaces (5–10). Prospective applications include self-cleaning and antifouling surfaces (1, 4, 6, 11) and textiles (12, 13), membranes for oil–water separation (14), and drag reduction in microfluidics (15). Superhydrophobic coatings can enhance (16) or reduce (17) adsorption of cells or proteins. Minute amounts of proteins or biomolecules can be deposited on arrays of micropillars, offering promising routes to sensitive high-throughput analysis on laboratory-on-chip benches (18). Patterned superhydrophobic coatings provide new strategies to guide drops (19) or to tune drop adhesion (20). Nanocrystals can be deposited (21) and grown (22) on the tips of a micropillar arrays. For all these applications, the robustness of a coating against complete wetting is crucial.

To fabricate a superhydrophobic surface, two key features are required: a low surface energy of the material and a topography with roughness on the nanoscale and microscale. In this case, air can be entrained when placing a sessile drop on top, which leads to the low adhesion. In this so-called Cassie or fakir state, the drop rests on top of the asperities of the rough substrate (Fig. 1*B*). As proposed by Cassie and Baxter (23, 24), a water drop on a partially wetted surface should adopt an apparent contact angle θ^{app} given by the weighted sum $\cos\theta^{app} = f\cos\theta - (1-f)$ (15, 24–27). Here, f denotes the fractional area of contact of water with the solid. θ is the contact angle on a flat surface of the same material. In the following, we distinguish between the macroscopically observed apparent contact angle and the material contact angle. The apparent contact angle is the one observed by eye or with a low-resolution microscope. It relates to a length scale much larger than the microstructures forming the superhydrophobic layer, thus typically larger than 10 μm. The material contact angle is the contact angle formed by the liquid on a smooth surface. It is derived by extrapolating the liquid shape on the 10 nm to 2 μm scale to the interface. The actual materials contact angle at the contact line θ_{CL} has to be between the advancing and receding ones: $\theta_{rec} \le \theta_{CL} \le \theta_{adv}$. The Cassie state competes with the Wenzel (impaled) state, in which the drop follows the topography of the surface and no air is entrapped (28, 29). The apparent contact angle in the Wenzel state can be almost as high as the one in the Cassie state (30). However, the two wetting states differ in the contact angle hysteresis, which is much lower in the Cassie state (31). Because the Cassie state minimizes the adhesion and the roll-off angle, the term Cassie state is often used as synonym for superhydrophobicity (14).

The Cassie-to-Wenzel transition can be triggered by vibrations (32), squeezing (10), impact (33), rapid deceleration (34), application of an electric field (35), or evaporation (33, 36–39). Different impalement scenarios have been discussed. For situations in which inertia is negligible, the two most important ones are depinning and sagging (31, 34–36, 38–43). In depinning, the three phase contact line, or briefly contact line, unpins from the edge of the asperity (37). Then the contact line slides down the pillar wall, beginning the transition to a fully wetted state. In the sag mechanism, the underside of the liquid surface sags until it reaches the substrate (36). The Cassie-to-Wenzel transition takes place as soon as the lowest point of the meniscus touches the bottom surface (31, 40). To simplify the discussion, we discriminate between the "contact line" on the microscopic and the "rim" on the macroscopic length scale.

Despite well-defined model systems, the transition dynamics is still poorly understood due to difficulties in monitoring the temporal evolution of the air cushion and the liquid–air meniscus between the asperities with sufficient special resolution (44). Even the timescale of the impalement transition remains unclear. So far, most detailed information was obtained by high-speed video microscopy (18, 40) and scanning electron microscopy (18, 25). However, neither of these techniques provides quantitative 3D information. Detailed insight in the transition dynamics would sharpen the fundamental understanding of superhydrophobicity and be constitutive to optimize the robustness of superhydrophobic coatings. Here, we study the Cassie-to-Wenzel transition of water drops evaporating on arrays of hydrophobic micropillars (Fig. 1*A*). The transition dynamics and especially the evolution of the thickness of the air cushions are monitored by laser scanning confocal microscopy (briefly confocal microscopy). The shape of the water–air cushion interface between the pillars and up to 200 μm above the substrate is imaged. Thus, we can measure both the macroscopic contact angle and the variation of the microscopic angle at the pillars. By varying the geometry of the substrate, we observe the impalement transition in both depinning and sagging modes.

Author contributions: P.P., D.V., and H.-J.B. designed research; P.P. performed research; L.M. and X.D. contributed new reagents; P.P. analyzed data; and P.P., D.V., and H.-J.B. wrote the paper.

The authors declare no conflict of interest.

This article is a PNAS Direct Submission.

[1]To whom correspondence should be addressed. E-mail: vollmerd@mpip-mainz.mpg.de.

This article contains supporting information online at www.pnas.org/lookup/suppl/doi:10.1073/pnas.1218673110/-/DCSupplemental.

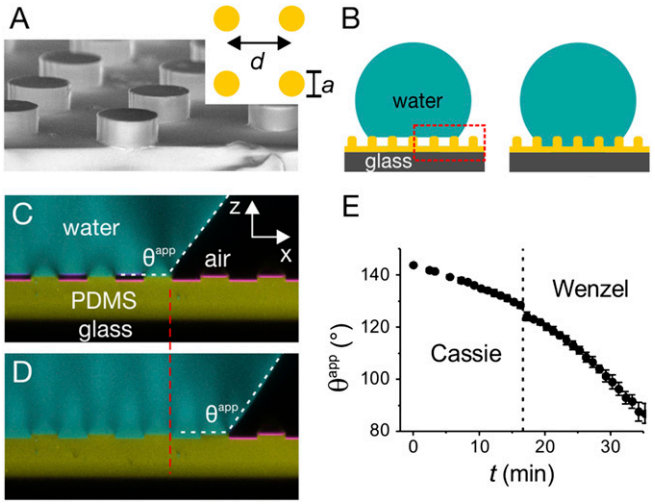

Fig. 1. Model superhydrophobic surfaces. (*A*) Scanning electron microscopy image of a microstructured PDMS surface. Dimensions of the pillars: center-to-center distance $d = 40$ μm, diameter $a = 20$ μm, and height $h = 5$ μm, giving $f_{PDMS} = 0.2$. (*B*) Sketch of a drop deposited on the substrate in the Cassie (*Left*) and Wenzel (*Right*) state. (*C*) Typical confocal microscopy image of a vertical section of a water drop rim just before and (*D*) just after the Cassie-to-Wenzel transition induced by evaporation. Fluorescent emission from water and PDMS is shown in cyan and yellow, respectively, and reflection in magenta. (*E*) Change of the apparent contact angle θ^{app} with time.

Results and Discussion

Cassie-to-Wenzel Transition. A fluorescently labeled water drop is left to evaporate on a labeled array of poly(dimethylsiloxane) (PDMS) pillars (Fig. 1). The superposition of the fluorescence and reflection images accurately depicts the morphology of the water–air and pillar–air interfaces (Fig. 1 *C* and *D*). Vertical sections of a drop in the Cassie state (Fig. 1*C*) show two well-separated horizontal reflections between neighboring pillars. They result from light reflected at the PDMS–air and air–water interfaces. The space in between (black regions) is filled with air. The height difference of the two reflections denotes the thickness of the air cushion. As water evaporates, the apparent contact angle decreases. The rim is pinned and the drop remains in the Cassie state (Fig. 1*E*). Only when the apparent contact angle reaches $\theta^{app} = 128°$, the drop suddenly wets the space between the pillars (Movie S1). The absence of reflection, supported by the fluorescence images of water and PDMS, proves the complete wetting of pillars, without entrained air (Fig. 1*D*).

The Cassie-to-Wenzel transition is accompanied by a decrease of the apparent contact angle by 3°. The rim jumped outwards so that the volume of the drop, V, was conserved. Assuming a spherical cap shape with radius R, the contact radius is as follows (Fig. S1):

$$b = R\sin\theta^{app} = \left(\frac{3V}{\pi}\right)^{1/3} \frac{\sin\theta^{app}}{(\cos^3\theta^{app} - 3\cos\theta^{app} + 2)^{1/3}}.$$

A jump of θ^{app} from 128° to 125° leads to an increase of b by 4.7%. The actual rim of the drop resembles an octagon with rounded edges (28). The maximum radius of the contact area jumps from 960 to 1,000 μm. This increase of 4.2% is close to the calculated value. The contact line remains pinned during further evaporation, while the contact angle decreases continuously.

Sag Impalement. To analyze the kinetics of the Cassie-to-Wenzel transition in more detail, we use microarrays with larger height and spacing between the pillars. Although PDMS pillars are frequently used (33), high PDMS pillars easily deform under capillary forces. Therefore, we use stiffer SU-8 pillars for these experiments. Fig. 2 shows a typical drop in the Cassie state. Because we did not fluorescently label the water in this case, the surface of the drop is detected from reflections. The almost spherical drop rests on 37 pillars. More than 100 horizontal sections of the reflection of light vertically spaced by 0.25 μm are combined in a 3D image (Fig. 2*B*). The mean curvature of the drop $1/R$ is governed by the Laplace pressure $P = 2\gamma/R$, where $\gamma = 72$ mN/m is the surface tension of water. Flattening of the drop by gravity is small because the radius of the drop $R < 1$ mm is much smaller than the capillary length of 2.7 mm.

To quantify the decreasing thickness of the air cushion h_{air} during evaporation, we extracted contour plots of the water–air interface (Fig. 2*C*). The variation of h_{air} along the main axis and the diagonal is included (Fig. 2*D*). The lowest height h_{min} is located at the center of each square, whereas a saddle point is formed along the main axis. The minimum of h_{air} along the main

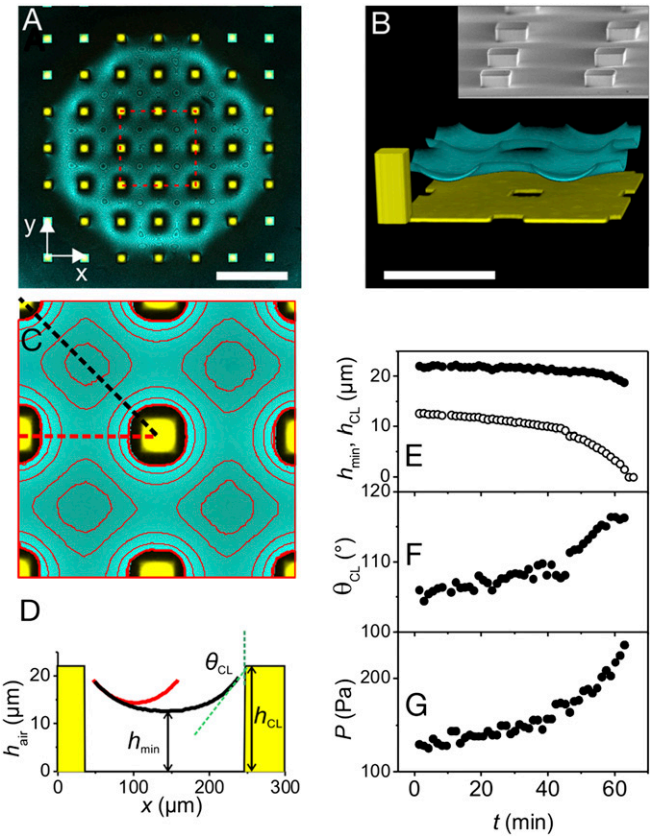

Fig. 2. Cassie-to-Wenzel transition via sagging. (*A*) Reflection from the water–air cushion interface (blue) of a droplet deposited on the microstructured surface composed of SU-8 pillars (yellow squares) taken by confocal microscopy. (Scale bar: 400 μm.) This horizontal section through the drop is taken 2 μm below the pillar surface. Dimensions of the pillars are as follows: $d = 200$ μm, $a = 50$ μm, and $h = 23$ μm. (*B*) Three-dimensional image of the reflection of light from the SU-8–air and air–water interfaces. (Scale bar: 200 μm.) An artificial pillar is shown for comparison (Movie S2). The z axis is 5× magnified. (*Inset*) SEM image of the pillars. (*C*) Contour plot of the thickness of the air cushion. The minimum thickness h_{min} is located at the center between four pillars. Contour lines corresponding to $h_{air} = 19$, 17, 15, and 13 μm are shown. (*D*) Variation of the thickness of the air cushion along the diagonal (black) and main axis (red). The two axes are marked in *C*. The contact angle θ_{CL} obtained from extrapolating the thickness of the air cushion to the edge of the pillars is indicated. (*E*) Change of h_{min} (hollow circles) and the thickness of the water–air cushion at the three phase contact line h_{CL} (solid circles) with time. (*F*) Change of θ_{CL} and (*G*) Laplace pressure P with time.

axis is almost 2 μm higher than the minimal height of the air cushion along the diagonal. From the respective variation of h_{air}, the contact angle of water at the contact line θ_{CL} can be derived (Fig. S2). It is maximal along the diagonal. This is the material contact angle, which can vary in the range $\theta_{rec} - 90° \leq \theta_{CL} \leq \theta_{adv}$ according to Gibbs' criterion, if measured from the vertical (28). In this case $\theta_{CL} = 106°$ just after deposition of the drop.

As evaporation proceeds, the curvature of the drop decreases and the Laplace pressure increases. The Laplace pressure of the drop is extracted from the mean curvature of the surface by fitting the water–air interface coordinates with a 2D function (Fig. S3). The water–air interface below the drop sags downward, the air cushion decreases and the contact angle θ_{CL} increases (Fig. 2 *E* and *F*). The water–air interface remains pinned, because the large pillar spacing prevents θ_{CL} from exceeding the advancing material contact angle, $\theta_{adv} = 115°$ (Fig. 2*F*) (44). The evolution of the 3D shape of the water–air interface is shown in Movie S2. At the first contact of the drop with the substrate, i.e., $h_{min} = 0$, the drop spontaneously wets the full surface within milliseconds. The Laplace pressure just before the transition is 250 Pa.

Depinning Impalement. With decreasing interpillar distance, it becomes more likely that θ_{CL} exceeds its maximum value θ_{adv} before the water–air interface touches the substrate. The snapshot in Fig. 3*A* shows the beginning of a depinning impalement (Movie S3). Depinning does not proceed simultaneously from all pillars but depends on detailed differences of the surface structure at the edge of the pillars. During impalement, the size of the drop and accordingly the pressure hardly change. Gradually, the curvature of the water–air interface beneath the drop increases (Fig. 3 *B* and *C*). Therefore, θ_{CL} varies between pillars. The contact line slides downward with an average speed of 0.5 μm/s until the drop touches the bottom surface and wets the whole substrate spontaneously.

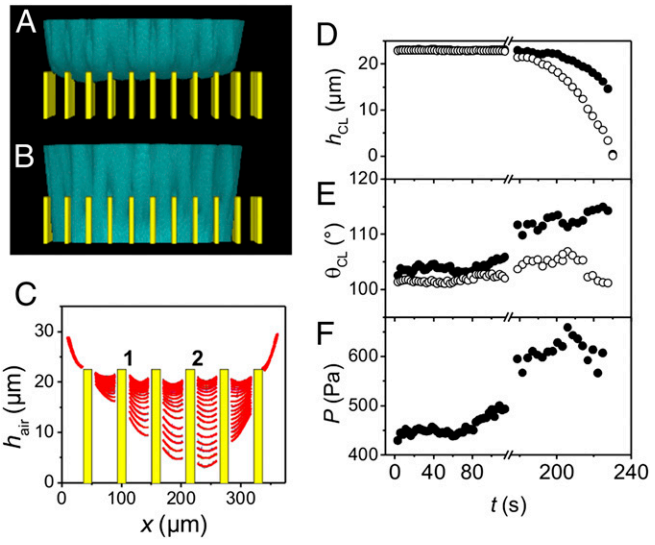

Fig. 3. Cassie-to-Wenzel transition via depinning. (*A*) Three-dimensional image of a fluorescently labeled water drop on an array of SU-8 pillars ($d = 20$ μm, $a = 5$ μm, $h = 5$ μm, z axis is 10× magnified). A 3D image ($300 \times 300 \times 20$ μm^3) was recorded every 0.90 s. For better visualization, we replace the microscopic data of the fluorescently labeled pillars by artificial pillars (Fig. S4). (*B*) The same drop after the collapse of the Cassie state. (*C*) Profiles of the thickness of the air cushion measured along a diagonal and passing through the center of the drop. Profiles are measured every 3 s ($d = 40$ μm, $a = 10$ μm, $h = 23$ μm). (*D*) Change of the height of the contact line at the side walls of the two pillars marked in *C*: **1** (solid circles) and **2** (hollow circles). (*E*) Change of the microscopic contact angle θ_{CL} during evaporation; position **1** (solid circles) and **2** (hollow circles) and (*F*) Laplace pressure *P* with time.

This velocity corresponds to the rate at which the drop evaporates. The radius of curvature of the drop decreases at roughly 0.7 μm/s close to the transition.

Simulations of drop collapse showed that the drop tends to acquire an overall spherical shape, outside and inside the substrate, and impalement does not cause a jump of the drop rim (44). Indeed, if impalement proceeds via depinning, it does not need not to be accompanied by a jump of the rim (Fig. 3*B* and Movie S3). According to our observations, the rim jumps if the receding angle of the Cassie state exceeds the advancing angle of the wetted (Wenzel) state, which depends on the height and shape of the pillars. Therefore, a jump of the contact line is more likely if the Cassie-to-Wenzel transition proceeds via sagging than via depinning.

Contact Angle Hysteresis. Finally, we discuss whether a drop in the Cassie state always shows a low contact angle hysteresis. This would imply that a surface that keeps drops in the Cassie state is superhydrophobic (37). However, even for the array with 200-μm pillar–pillar distance (Fig. 2; solid fraction $f = 6\%$) the drops show a high roll-off angle of α = 17° (Movie S4). The reason for the high roll-off angle becomes clear when watching the rim of a drop more closely as water evaporates (Fig. 4). Immediately after deposition, the drops are almost spherical, although pinning at the edges of a few pillars is visible (Fig. 4*A*). As water evaporates, the drop depins stepwise from the top of the pillars (Movie S5). Tiny water droplets are left on the top of the pillars (18, 21) (Movie S6). The time between successive depinning events varies between <1 s and 10 min. When the bottom surface of the drop gets into contact with the substrate, the whole drop spontaneously undergoes a Cassie-to-Wenzel transition. The contact line jumps outward (Fig. 4 *B* and *C*). Part of the air remains trapped at the backside of the pillars with respect to the flow profile (Fig. 4*C Inset*). Thus, from the position of the bubbles with respect to the pillar, the first contact can be localized. The size of the bubbles continuously decreases by diffusion through the water phase until after about 10 min the bubbles disappear.

The images show that wetting is dominated by pinning rather than thermodynamic equilibrium. The Cassie–Baxter equation cannot be valid because the drop is in a metastable state. Choi et al. (25) suggested a modified Cassie–Baxter equation to calculate the advancing and receding contact angles. Their model is based on the calculation of the local maxima and minima of the interfacial energy. For the receding contact angles on discrete pillars, the solid areal fraction is essentially replaced by the solid line fraction. Reyssat and Quéré (45) followed a geometric approach to estimate the receding contact angle, based on the equivalence of macroscopic and microscopic pinning forces.

With θ_{CL} measured at each pillar by confocal microscopy, the apparent contact angle can be calculated from the following balance of forces: the macroscopic horizontal component of the interfacial force at the rim per unit length is $F_{app,h} = \gamma(1 + \cos\theta^{app})$ (Fig. 4*D*). This force is made up of the force of the individual pillars. Microscopically, each pillar supports a horizontal component of the pinning force of $\gamma a \cos\theta_{rec}$ at the rear side and nearly γa at the front side (for large drops $\theta_{CL} \approx 90°$; Figs. 2 and 3) until just before depinning. If the contact line is pinned, this leads to the following:

$$\gamma d(1 + \cos\theta^{app}) = \gamma a(\cos\theta_{rec} + 1) \Rightarrow \cos\theta^{app} = \frac{a}{d}(\cos\theta_{rec} + 1) - 1$$

with respect to a movement along the main axis. With $d = 200$ μm, $a = 50$ μm, and $\theta_{rec} = 85°$, we get $\theta^{app} = 137°$. This compares well to the measured value of 135°. Our approach can take the finite size of a drop and variations of the contact line into account. The horizontal pinning force per pillar is 3.9 μN.

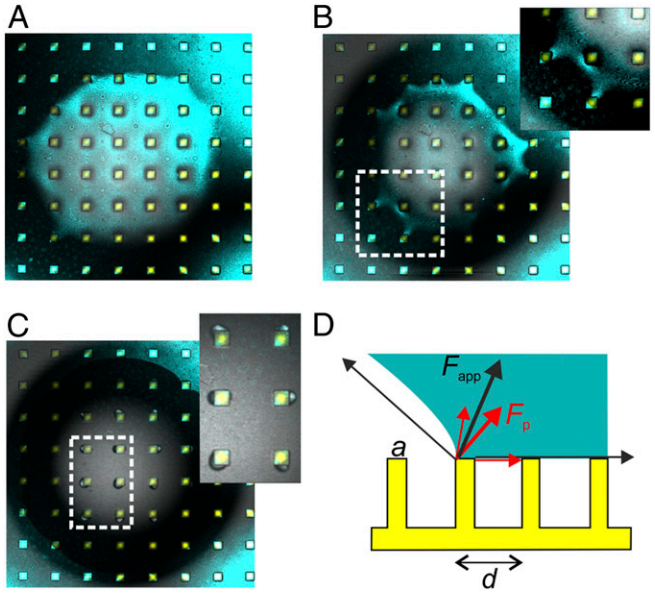

Fig. 4. Drop depinning during evaporation. (*A*) Superposition of transmission (bluish) and the reflection from the drop–air cushion interface (cyan) on SU-8 pillars (yellow) (d = 200 μm, a = 50 μm, h = 25 μm) just after deposition. (*B*) Rim of the drop just before the impalement transition. (*Inset*) Pinning-induced necks of the drop. (*C*) Horizontal section recorded just after the impalement transition. (*Inset*) Air bubbles are visible at the backside of the pillars. (*D*) Macroscopic pinning force F_{app} at the receding part of the drop rim (black arrows). Its horizontal component must be equal to the sum of horizontal components of pinning forces F_p at the pillars (red arrows). It is assumed that the mean curvature of the drop is zero.

This pinning force also provides an estimate for the roll-off angle α. Therefore, we compare the pinning force to the force caused by the weight when tilting the plate (45). The component of the weight of the drop parallel to the surface is $F_{\|} = V\rho g \sin\alpha$. Setting both forces equal leads to a roll off angle α of the following:

$$V\,\rho\,g\,\sin\alpha = n\gamma a(\cos\theta_{rec}+1) \Rightarrow \sin\alpha = \frac{n\gamma a}{V\rho g}(\cos\theta_{rec}+1).$$

Here, n is the numbers of pillars holding the drop. With a drop volume $V = 6$ μL, the roll-off angle is α = 4° for $n = 1$ and 19° for $n = 5$. The latter is more plausible for a drop of this size (Figs. 2 and 3), hinting that for larger drops the roll-off angle is affected by simultaneous depinning from several pillars. Consequently, a stable Cassie state and a high apparent contact angle do not necessarily imply a low roll-off angle and superhydrophobicity.

Conclusions

We image the collapse of the Cassie state for a series of model surfaces. By confocal microscopy, details of the impalement dynamics are resolved. In particular, the evolution of the thickness of the air cushion can be recorded in three dimensions. Depending on the geometry, impalement can extend over several minutes. The downward velocity of the meniscus is related to the evaporation rate. When the drops recede, we observe single depinning events and the formation and the breakage of finger-like necks. Calculated apparent receding contact and roll-off angles agree well with the measured data. We expect that confocal microscopy will become a standard technique to characterize superhydrophobic surfaces, because this time-resolved 3D information can be gained for every transparent substrate

Materials and Methods

Lithography. Microarrays consisting of flat-top cylindrical pillars made of PDMS (Fig. 1*A*) and rectangular pillars made of SU-8 photoresist (Fig. 2 *A* and *B*) were fabricated using lithography (*SI Materials and Methods*). Both were arranged on glass in a square lattice of center-to-center distance d. The corresponding surface fractions are $f_{PDMS} = \frac{\pi}{4}(a/d)^2$ and $f_{SU-8} = (a/d)^2$. Here, a denotes the diameter (PDMS) or edge length (SU-8), respectively (Figs. 1*A* *Inset* and 2 *A* and *B*). The surface of the SU-8 pillars was coated with a semifluorinated silane to decrease the surface energy. Advancing and receding contact angles for water on flat parts of the surface were $\theta_{adv} = 112 \pm 2°$, $\theta_{rec} = 70 \pm 10°$ on PDMS, and $\theta_{adv} = 118 \pm 2°$, $\theta_{rec} = 85 \pm 5°$ on SU-8. Hydrophobic perylenemonoimide dye (PMI) (emission maximum at $\lambda_{PMI} = 540$ nm) was added to un–cross-linked PDMS or SU-8 (28). Water-soluble perylenediimide (WS-PDI) was used to dye the water because of its negligible interfacial activity.

Laser Scanning Confocal Microscopy. To visualize the Cassie and Wenzel state and to record the impalement dynamics, we deposited 7-μL water drops on the micropatterned surfaces (Fig. 1*B*). The confocal microscope used (Leica TCS SP5 II – STED CW) has five detectors with adjustable spectral regions, which allowed us to simultaneously measure fluorescence from water and PDMS or SU-8, as well as the reflected light from the interfaces (Fig. 1 *C* and *D*) (28). To verify that the results are not influenced by the dye (46, 47), some measurements were repeated with pure water in reflection mode. A dry objective (40×/0.85) was used because it allows to accurately measure the optical path length in air, i.e., the thickness of the air cushion. The image resolution was about 0.25 and 1.0 μm in the horizontal and vertical directions, respectively, except for areas closer than about 0.1d to the edges of the pillars. The coordinates of the water–air interface are extracted by fitting reflection or fluorescence profiles along the z axis with a Gaussian or sigmoidal function, respectively, with accuracy better than 0.3 μm.

ACKNOWLEDGMENTS. We thank A. Kaltbeizel, F. Schellenberger, and J. Morsbach for technical support, and J. Yeomans, C. Sembrebon, and M. Klapper for discussions. We also thank K. Landfester for providing the confocal microscope. Financial support is gratefully acknowledged from Schwerpunktprogramm 1420 (H.-J.B.), Deutsche Forschungsgemeinschaft Bu 1556/27 (H.-J.B.), Schwerpunktprogramm 8173 (D.V.), and Sonderforschungsbereich-TR6 (P.P).

1. Barthlott W, Neinhuis C (1997) Purity of the sacred lotus, or escape from contamination in biological surfaces. *Planta* 202(1):1–8.
2. Gao XF, Jiang L (2004) Biophysics: Water-repellent legs of water striders. *Nature* 432(7013):36.
3. Parker AR, Lawrence CR (2001) Water capture by a desert beetle. *Nature* 414(6859): 33–34.
4. Wagner T, Neinhuis C, Barthlott W (1996) Wettability and contaminability of insect wings as a function of their surface sculptures. *Acta Zoologica* 77(3):213–225.
5. Feng L, et al. (2002) Super-hydrophobic surfaces: From natural to artificial. *Adv Mater* 14(24):1857–1860.
6. Li X-M, Reinhoudt D, Crego-Calama M (2007) What do we need for a superhydrophobic surface? A review on the recent progress in the preparation of superhydrophobic surfaces. *Chem Soc Rev* 36(8):1350–1368.
7. Feng X, Jiang L (2006) Design and creation of superwetting/antiwetting surfaces. *Adv Mater* 18(23):3063–3078.
8. Roach P, Shirtcliffe NJ, Newton MI (2008) Progess in superhydrophobic surface development. *Soft Matter* 4(2):224–240.
9. Xia F, Jiang L (2008) Bio-inspired, smart, multiscale interfacial materials. *Adv Mater* 20(15):2842–2858.
10. Yao X, et al. (2010) Bioinspired ribbed nanoneedles with robust superhydrophobicity. *Adv Funct Mater* 20(4):656–662.
11. Deng X, et al. (2011) Transparent, thermally stable and mechanically robust superhydrophobic surfaces made from porous silica capsules. *Adv Mater* 23(26):2962–2965.
12. Artus GRJ, Zimmermann J, Reifler FA, Brewer SA, Seeger S (2012) A superoleophobic textile repellent towards impacting drops of alkanes. *Appl Surf Sci* 258(8):3835–3840.
13. Zhou H, et al. (2012) Fluoroalkyl silane modified silicone rubber/nanoparticle composite: A super durable, robust superhydrophobic fabric coating. *Adv Mater* 24(18):2409–2412.
14. Kota AK, Kwon G, Choi W, Mabry JM, Tuteja A (2012) Hydro-responsive membranes for effective oil-water separation. *Nat Commun* 3:1025.
15. Quere D (2005) Non-sticking drops. *Rep Prog Phys* 68(11):2495–2532.
16. Shiu JY, Kuo CW, Whang WT, Chen PL (2010) Observation of enhanced cell adhesion and transfection efficiency on superhydrophobic surfaces. *Lab Chip* 10(5):556–558.
17. Koc Y, et al. (2008) Nano-scale superhydrophobicity: Suppression of protein adsorption and promotion of flow-induced detachment. *Lab Chip* 8(4):582–586.
18. Dufour R, et al. (2012) Zipping effect on omniphobic surfaces for controlled deposition of minute amounts of fluid or colloids. *Small* 8(8):1229–1236.
19. Mertaniemi H, et al. (2011) Superhydrophobic tracks for low-friction, guided transport of water droplets. *Adv Mater* 23(26):2911–2914.

20. Hong X, Gao X, Jiang L (2007) Application of superhydrophobic surface with high adhesive force in no lost transport of superparamagnetic microdroplet. *J Am Chem Soc* 129(6):1478–1479.
21. Krumpfer JW, McCarthy TJ (2011) Dip-coating crystallization on a superhydrophobic surface: A million mounted crystals in a 1 cm2 array. *J Am Chem Soc* 133(15):5764–5766.
22. Hatton BD, Aizenberg J (2012) Writing on superhydrophobic nanopost arrays: Topographic design for bottom-up assembly. *Nano Lett* 12(9):4551–4557.
23. Cassie ABD, Baxter S (1945) Large contact angles of plant and animal surfaces. *Nature* 155(3923):21–22.
24. Cassie ABD, Baxter S (1944) Wettability of porous surfaces. *Trans Faraday Soc* 40: 0546–0550.
25. Choi W, Tuteja A, Mabry JM, Cohen RE, McKinley GH (2009) A modified Cassie-Baxter relationship to explain contact angle hysteresis and anisotropy on non-wetting textured surfaces. *J Colloid Interface Sci* 339(1):208–216.
26. Extrand CW (2004) Criteria for ultralyophobic surfaces. *Langmuir* 20(12):5013–5018.
27. Extrand CW (2002) Model for contact angles and hysteresis on rough and ultraphobic surfaces. *Langmuir* 18(21):7991–7999.
28. Papadopoulos P, et al. (2012) Wetting on the microscale: Shape of a liquid drop on a microstructured surface at different length scales. *Langmuir* 28(22):8392–8398.
29. Verho T, et al. (2012) Reversible switching between superhydrophobic states on a hierarchically structured surface. *Proc Natl Acad Sci USA* 109(26):10210–10213.
30. Wenzel RN (1936) Resistance of solid surfaces to wetting by water. *Ind Eng Chem* 28(8):988–994.
31. Lafuma A, Quéré D (2003) Superhydrophobic states. *Nat Mater* 2(7):457–460.
32. Bormashenko E, Pogreb R, Whyman G, Erlich M (2007) Cassie-Wenzel wetting transition in vibrating drops deposited on rough surfaces: Is the dynamic Cassie-Wenzel wetting transition a 2D or 1D affair? *Langmuir* 23(12):6501–6503.
33. Bartolo D, et al. (2006) Bouncing or sticky droplets: Impalement transitions on superhydrophobic micropatterned surfaces. *Europhys Lett* 74(2):299–305.
34. Kwon H-M, Paxson AT, Varanasi KK, Patankar NA (2011) Rapid deceleration-driven wetting transition during pendant drop deposition on superhydrophobic surfaces. *Phys Rev Lett* 106(3):036102.
35. Manukyan G, Oh JM, van den Ende D, Lammertink RGH, Mugele F (2011) Electrical switching of wetting states on superhydrophobic surfaces: A route towards reversible Cassie-to-Wenzel transitions. *Phys Rev Lett* 106(1):014501.
36. Reyssat M, Yeomans JM, Quere D (2008) Impalement of fakir drops. *Europhys Lett* 81(2):26006.
37. Kusumaatmaja H, Blow ML, Dupuis A, Yeomans JM (2008) The collapse transition on superhydrophobic surfaces. *Europhys Lett* 81(3):36003.
38. McHale G, Aqil S, Shirtcliffe NJ, Newton MI, Erbil HY (2005) Analysis of droplet evaporation on a superhydrophobic surface. *Langmuir* 21(24):11053–11060.
39. Kwon DH, Lee SJ (2012) Impact and wetting behaviors of impinging microdroplets on superhydrophobic textured surfaces. *Appl Phys Lett* 100(17):171601.
40. Tsai P, Lammertink RGH, Wessling M, Lohse D (2010) Evaporation-triggered wetting transition for water droplets upon hydrophobic microstructures. *Phys Rev Lett* 104(11):116102.
41. Dorrer C, Ruhe J (2009) Some thoughts on superhydrophobic wetting. *Soft Matter* 5(1):51–61.
42. Whyman G, Bormashenko E, Stein T (2008) The rigorous derivation of Young, Cassie-Baxter and Wenzel equations and the analysis of the contact angle hysteresis phenomenon. *Chem Phys Lett* 450(4-6):355–359.
43. Susarrey-Arce A, et al. (2012) Absence of an evaporation-driven wetting transition on omniphobic surfaces. *Soft Matter* 8(38):9765–9770.
44. Oliver JF, Huh C, Mason SG (1977) Resistance to spreading of liquids by sharp edges. *J Colloid Interface Sci* 59(3):568–581.
45. Reyssat M, Quéré D (2009) Contact angle hysteresis generated by strong dilute defects. *J Phys Chem B* 113(12):3906–3909.
46. Luo C, et al. (2010) Direct three-dimensional imaging of the buried interfaces between water and superhydrophobic surfaces. *Angew Chem Int Ed Engl* 49(48): 9145–9148.
47. Wu J, Zhang M, Wang X, Li S, Wen W (2011) A simple approach for local contact angle determination on a heterogeneous surface. *Langmuir* 27(10):5705–5708.